Control of NTMs and integrated multi-actuator plasma control on TCV

M Kong[1], T C Blanken[2], F Felici[1], C Galperti[1], E Maljaars[2], O Sauter[1], T Vu[1], F Carpanese[1], A Merle[1], J-M Moret[1], F Pesamosca[1], E Poli[3], M Reich[3], A A Teplukhina[1‡], the TCV team[§] and the EUROfusion MST1 Team[‖]

[1]École Polytechnique Fédérale de Lausanne (EPFL), Swiss Plasma Center (SPC), CH-1015 Lausanne, Switzerland

[2]Eindhoven University of Technology, Department of Mechanical Engineering, PO Box 513, 5600MB Eindhoven, the Netherlands

[3]Max-Planck Institut für Plasmaphysik, Garching, Germany

E-mail: `mengdi.kong@epfl.ch`

January 2019

Abstract. The control of 2/1 neoclassical tearing modes (NTMs) with electron cyclotron (EC) waves has been studied both experimentally and numerically on TCV. Dynamic evolutions of NTMs along with time-varying deposition locations of the control beam have been studied in detail. The prevention of NTMs by means of preemptive EC (i.e. the control beam is switched on before the mode onset) has also been explored. A small sinusoidal sweeping with full amplitude of 0.07 (normalized to the minor radius) has been added to the control beam in two of the experiments to facilitate the comparison between NTM stabilization and prevention. It is shown that the prevention of NTMs is more efficient than NTM stabilization in terms of the minimum EC power required. Interpretative simulations with the Modified Rutherford Equation (MRE) have been performed to better quantify various effects, with coefficients well defined by dedicated experiments. Specifically, in order to obtain more insight on the dominant dependencies, a simple ad-hoc analytical model has been proposed to evaluate the time-varying classical stability index Δ' in the test discharges, based on the Δ'-triggered nature of these 2/1 NTMs. This allows simulating well the entire island width evolution with the MRE, starting from zero width and including both NTM stabilization and prevention cases for the first time. The exploration of NTM physics and control has facilitated the development of an NTM controller that is independent of the particular features of TCV and has been included in a generic plasma control system (PCS) framework. Integrated control of 2/1 NTMs, plasma β (the ratio of plasma pressure to magnetic pressure) and model-estimated safety factor q profiles has been demonstrated on TCV.

Keywords: NTM stabilization and prevention, Modified Rutherford Equation (MRE),

‡ Present address: Princeton Plasma Physics Laboratory, Princeton, NJ 08543, USA.

§ See the author list of S. Coda et al., 2017 Nucl. Fusion 57 102011.

‖ See the author list of H. Meyer et al., 2017 Nucl. Fusion 57 102014.

integrated control

1. Introduction

Neoclassical tearing modes (NTMs) located at the $m = 2$, $n = 1$ rational surface (where m and n are the poloidal and toroidal mode number respectively) can cause more than 20% confinement degradation, decrease the Q factor (ratio between the fusion and auxiliary heating powers) and lead to plasma disruptions, especially in high confinement mode (H-mode) plasmas [1, 2]. This is beyond the acceptable level for ITER, highlighting the importance of better understanding the physics of NTMs and their reliable control. Given its highly localized deposition, electron cyclotron (EC) wave has proven to be promising in the effective control of NTMs and will be used in ITER [3,4]. The effect of EC beams on the stability and control of NTMs is twofold: by modifying the current density profile and thus the stability index of the TM (Δ'), and by replacing the missing bootstrap current within the magnetic island through direct current drive (ECCD) or indirect heating effect (ECH) [5].

Much theoretical work has been performed to clarify the effects of various terms on the evolution of the island width, either with the Modified Rutherford Equation (MRE) [1–3, 5–7, and references therein] or the MHD model [8–10, and references therein]. Meanwhile, experimental studies concerning the stabilization and prevention of NTMs have been performed on several tokamaks [1, 11–16, and references therein], mostly about 3/2 NTMs and a few on 2/1 NTMs. Although similar physics is involved in 3/2 and 2/1 NTMs, the control of 2/1 NTMs is more challenging due to their typically larger growth rate and proximity to the plasma edge, which on one hand increases the chance of mode locking and disruptions and on the other hand decreases the ECCD efficiency. The reliable and efficient control of 2/1 NTMs is thus a major concern for ITER and needs to be ensured. In this respect, more experimental efforts are still needed to carefully isolate different effects, assess the range of validity of theoretical models and improve the control algorithms.

In this paper, dedicated experiments on the control of 2/1 NTMs on TCV and interpretative modeling with the MRE are presented. With the relatively short time scale of TCV (confinement time $\sim$ 5ms and resistive time $\sim$ 100ms) and its flexible EC system, different plasma conditions and various aspects of NTM control have been explored. For instance, dynamic evolutions of 2/1 NTMs along with time-varying deposition locations of the control beam have been studied in detail. The effect of co-ECCD (i.e. current drive in the same direction as plasma current), counter-ECCD (i.e. current drive in the opposite direction to plasma current) and ECH on the stabilization of 2/1 NTMs has been compared through a series of experiments as well as interpretative simulations with the MRE. A small sinusoidal sweeping of the radial deposition location of the EC power has been added to the control beam in two experiments (section 2.3.4) to facilitate the comparison between NTM stabilization and prevention, by improving the coverage of the correct location in both cases despite of different plasma evolutions.

It is shown that the prevention of NTMs is more efficient than NTM stabilization in terms of the minimum EC power required. The inclusion of the small sweeping allows one to develop a more reliable NTM controller since it reduces the difficulties caused by the inaccuracies of the equilibrium reconstruction that may vary with different plasma scenarios. A generic controller is thus developed and has been included in an integrated control scheme.

In the interpretative simulations, a simple analytical model is proposed to evaluate the time-varying Δ' in the test discharges, where 2/1 NTMs are anticipated to be triggered by unstable Δ' [17, 18] and typically referred to as "triggerless" or "seedless" NTMs in the literature [17, 19]. This for the first time allows the simulation of the entire island width evolution with the MRE, starting from zero width (i.e. no island) and including both NTM stabilization and prevention cases. Meanwhile, the inclusion of the various terms in the MRE (as will be detailed in section 2.2) and the capability of starting the simulation from a finite island width as in the literature [1–3, 7, 14, 20] facilitate the comparison of various effects and the validation of theoretical models, for both "seedless" and seeded NTMs.

The reliable and generic NTM controller can be readily integrated with other real-time (RT) algorithms needed for tokamak operation. For large devices like ITER, supervising the plasma discharge evolution and performing multiple control tasks sharing a limited set of actuators are essential [12]. This requires reliable RT plasma state reconstruction, monitoring and supervision [21], actuator management [22] and controllers [22–26]. With the NTM controller mentioned above and following a generic integrated control framework [21,22], integrated control of NTMs, β (the ratio of plasma pressure to magnetic pressure) and model-estimated safety factor (q) profiles has been demonstrated on TCV.

The rest of the paper is organized as follows. Section 2 details the experimental and numerical study of NTM physics and control on TCV. The plasma scenario and experimental setup are described in section 2.1, the MRE model is detailed in section 2.2, and the experimental and simulation results concerning NTM control (stabilization or prevention) are presented in section 2.3. Under section 2.3, section 2.3.1 discusses about the self-stabilization of NTMs through a slow ramp-down of the destabilizing power; section 2.3.2 presents the evolution of a 2/1 NTM along with a large variation of the deposition location of the control beam (between the plasma center and edge), constraining better the theoretical model used in the simulations; section 2.3.3 compares the effect of co-ECCD, counter-ECCD and ECH on the stabilization of 2/1 NTMs, with various effects quantified by detailed simulations with the MRE; section 2.3.4 compares the efficiency of NTM prevention with NTM stabilization, in terms of the minimum EC power required in each case. In section 3, RT integrated control of 2/1 NTMs, plasma β and model-estimated q profiles on TCV is demonstrated, along with an introduction to the generic PCS framework used in the experiment. Conclusions and outlook are summarized in section 4.

2. NTM physics and control

2.1. Plasma scenario and experimental setup

In these NTM control experiments on TCV, limited L-mode plasmas with constant plasma current ($I_p \approx 110$kA), toroidal magnetic field ($B_0 \approx 1.44T$), q_{95} (q at the 95% poloidal flux surface, $q_{95} \approx 7$), triangularity ($\delta \approx 0.25$ at the plamsa edge) and elongation ($\kappa \approx 1.32$ at the plamsa edge) are used. Relatively constant low density is kept in each test to ensure 100% absorption of EC beams. The line-averaged density (n_{el}) along the chord passing through the plasma center ranges from $1.4 \times 10^{19} m^{-3}$ to $2 \times 10^{19} m^{-3}$ in various experiments.

As illustrated in figure 1 (a), two second harmonic X-mode (X2) EC gyrotrons with a nominal power of 0.5MW each are applied to deposit power near the plasma center and drive current in the same direction as I_p (i.e. co-ECCD), using two launchers (named as $L4$ and $L6$) with independent steerable mirrors. About 40kA current can be driven with 1MW total power for the scenarios used here. 2/1 NTMs are typically destabilized about 100ms (i.e. the resistive time scale on TCV) after turning on these central EC powers, through a modification of the current density profile, i.e. a Δ' effect [17, 18]. The mode then grows neoclassically under the effect of perturbed bootstrap current (i.e. NTMs). A third X2 gyrotron with a nominal power of 0.75MW and an independent launcher ($L1$) is used for control purposes. The toroidal angles of these launchers are set before the experiment to allow for co-ECCD, counter-CD or ECH, while their poloidal angles can be controlled by feedforward or feedback commands to vary their deposition locations during the shot. The EC power and poloidal angle traces in the experiments presented in this section were pre-programmed, while the RT application of the NTM control scheme will be illustrated in section 3. EC-relevant parameters such as the power absorption rate, deposition location and driven current of the beams from each launcher are computed by the ray-tracing code TORAY-GA [27]. Shown in figure 1 (b) is an example of the deposited power density profiles of the three launchers.

As one component of the magnetic diagnostic system on TCV, four poloidal arrays of 38 magnetic probes each (marked as red rectangles in figure 1 (a)) are placed inside the vessel on four toroidal sectors separated by 90°. They measure the time derivative of the magnetic field tangential to the vessel with an acquisition frequency up to 500kHz. This allows the identification of the m and n number of a certain mode, its amplitude as well as its frequency. Specifically, the experimental island widths (w_{exp}) presented in this paper are estimated by fitting the helical flux perturbations to the measurements from the probes [28, 29] and have an error bar of about 20%. The plasma equilibrium is reconstructed by the Grad-Shafranov equilibrium solver LIUQE [30] while the local electron density and temperature are measured by a Thomson scattering system [31]. The measured and reconstructed data are then used by the transport code ASTRA [32] that solves relevant profiles such as q, magnetic shear and bootstrap current density consistently. Specifically, interpretative ASTRA simulations have been performed to solve the poloidal flux (Ψ) diffusion equation based on the temperature

and density measurements (thus the bootstrap current density), EC-relevant parameters from TORAY-GA (e.g. driven current densities from ECCD) as well as the equilibrium, with I_p as the boundary condition. Relevant ASTRA outputs are then used as inputs for the interpretative simulations with the MRE, as will be discussed in the following sections. The radial location (ρ) of a given mode can be determined by its m/n number from magnetic analyses and the $q(\rho)$ profile from ASTRA.

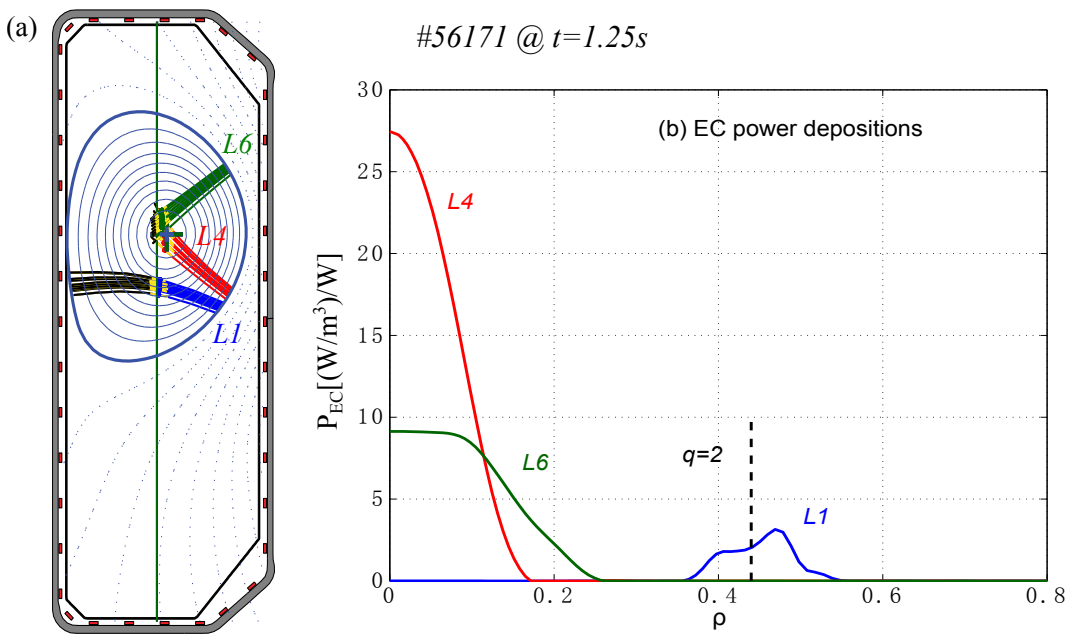

Figure 1: Illustration of the plasma scenario and experimental setup: (a) a poloidal cross section of TCV showing one poloidal array of 38 magnetic probes (red rectangles on the wall), flux surfaces computed by LIUQE and EC traces from TORAY; (b) deposited EC power density profiles per injected power computed by TORAY, with the $q = 2$ location from ASTRA marked as the dashed vertical line. The example is taken from shot #56171 at $t = 1.25s$.

2.2. Theoretical model

The MRE model is used to quantify the effect of different terms on the overall evolution of the island width w, and can be written as [3, 20, 33, 34]:

$$\frac{\tau_R}{\overline{\rho}_{mn}}\frac{dw}{dt} = \overline{\rho}_{mn}\Delta' + \overline{\rho}_{mn}\Delta'_{BS} + \overline{\rho}_{mn}\Delta'_{GGJ} + \overline{\rho}_{mn}\Delta'_{CD} + \overline{\rho}_{mn}\Delta'_{H}, \tag{1}$$

with

$$\overline{\rho}_{mn}\Delta'_{BS} = a_2\overline{\rho}_{mn}\beta_p\left|L_{bs}\right|\frac{L_q}{(-L_p)}\frac{w}{w^2+w_{de}^2} = a_2\overline{\rho}_{mn}\frac{2\mu_0 R_0 q_{mn}}{s_{mn}B_0}j_{bs,mn}\frac{w}{w^2+w_{de}^2}, \tag{2}$$

$$\overline{\rho}_{mn}\Delta'_{GGJ} = -a_3\overline{\rho}_{mn}\frac{6D_R}{\sqrt{w^2+0.2w_{de}^2}} = -a_3\frac{12\mu_0 R_0^2}{B_0^2}\frac{\epsilon_{mn}^2}{s_{mn}^2}\frac{p_{mn}}{(-L_p)}\frac{(q_{mn}^2-1)}{\sqrt{w^2+0.2w_{de}^2}}, \tag{3}$$

$$\overline{\rho}_{mn}\Delta'_{CD} = -a_4\frac{16\mu_0 R_0 q_{mn}}{\pi s_{mn}B_0}\sum_{j=1}^{nl}\frac{I_{cd,j}}{w_{dep,j}^2}N_{cd,j}(\frac{w}{w_{dep,j}})G_{cd,j}(\frac{w}{w_{dep,j}},\overline{\rho}_{dep,j})M_{cd,j}(\frac{w}{w_{dep,j}},D_j), \tag{4}$$

and

$$\overline{\rho}_{mn}\Delta'_H = -a_5\frac{16\mu_0 R_0 q_{mn}}{\pi s_{mn} B_0}\sum_{j=1}^{nl}\frac{\eta_{H,j}P_{l,j}}{w_{dep,j}^2}N_{H,j}(\frac{w}{w_{dep,j}})G_{H,j}(\frac{w}{w_{dep,j}},\overline{\rho}_{dep,j})M_{H,j}(\frac{w}{w_{dep,j}},D_j), \quad (5)$$

where a_2 to a_5 are constant "free" parameters to account for the assumptions in the model and the uncertainties in the data to fit the experimental results. a_2 is typically tuned based on the observed saturated island width (w_{sat}), and for example in reference [20] it was taken as 2.6 when assuming $\overline{\rho}_{mn}\Delta' = -m$; $\overline{\rho}_{mn}\Delta'_{GGJ}$ is typically small and a_3 has been fixed to 0.25 in the simulations involved in this paper; a_4 and a_5 can be determined through dedicated NTM stabilization experiments with co-ECCD, counter-ECCD and ECH beams as well as corresponding simulations, as will be detailed in section 2.3.3. Note that all of the three cases (co-ECCD, counter-ECCD and ECH) have a stabilizing heating effect (i.e. $\overline{\rho}_{mn}\Delta'_H < 0$) despite of different contributions to $\overline{\rho}_{mn}\Delta'_{CD}$.

The subscript "mn" in equation (2) - (5) represents the value evaluated at the $q = m/n$ rational surface; $\overline{\rho}$ is the radial location of flux surfaces defined by $\overline{\rho} = \sqrt{\frac{\Phi}{\Phi_{edge}}}\cdot a$, with Φ the toroidal flux contained by a given flux surface, Φ_{edge} the value at the plasma edge and a the minor radius ($0.25m$ for TCV); $\epsilon = a/R_0$, where R_0 is the major radius ($0.88m$ for TCV); $\tau_R = \frac{\mu_0\overline{\rho}_{mn}^2}{1.22\eta_{neo}}$ is the effective resistive time and η_{neo} the neoclassical resistivity at the rational surface [35,36]; β_p is the ratio of plasma pressure p to poloidal magnetic pressure $\frac{B_p^2}{2\mu_0}$, and has been replaced by $\beta_p = \frac{2\mu_0 p}{B_p^2} \approx \frac{2\mu_0 p_{mn}R_0^2 q_{mn}^2}{\overline{\rho}_{mn}^2 B_0^2}$ through the approximate relation between B_p and B_0 under the large aspect ratio assumption; $L_q^{-1} = \frac{1}{q}\frac{dq}{d\overline{\rho}} = s/\overline{\rho}$, where s is the magnetic shear; $L_p^{-1} = \frac{1}{p}\frac{dp}{d\overline{\rho}}$; $D_R = \frac{\epsilon^2\beta_p}{s}\frac{L_q}{-L_p}(1-\frac{1}{q^2})$; w_{de} accounts for the finite ratio of perpendicular to parallel heat transport ($\chi_\perp/\chi_\parallel$) at small w [37] and is given by [1,37]

$$w_{de} = \left[5.1(\frac{1}{\epsilon s n})^{\frac{1}{2}}\right]^{\frac{4}{3}}(\frac{\chi_\perp}{\chi_\parallel})^{\frac{1}{3}}\overline{\rho}_{mn}. \quad (6)$$

In equation (4) and (5), nl refers to the total number of EC launchers involved; I_{cd} is the driven current from a given EC launcher, P_l the absorbed power, $\overline{\rho}_{dep}$ the location of the peak of the deposited power density and w_{dep} the full e^{-1} width; η_H estimates the efficiency with which the EC power is converted into a perturbative inductive current and is given by $\eta_H = \frac{3w_{dep}^2}{8\pi R n_{e,mn}\chi_\perp}\frac{j_{sep}}{T_{sep}}$ [33], where $n_{e,mn}$ refers to the local electron density, j_{sep} refers to the inductive part of the current density at the island separatrix and T_{sep} is the corresponding electron temperature in eV. The $M_{cd,H}$ and D terms in equation (4) and (5) represent the effect of EC power modulation and the power on-time fraction, respectively, and both equal 1 for continuous wave injections used here; the $N_{cd,H}$ terms represent the dependence on w with $N_{cd} = 0.25[1+\frac{2}{3}(\frac{w}{w_{dep}})^2]^{-1}$ when assuming local continuous wave deposition [38] and N_H taken from equation (28) of reference [33]; the $G_{cd,H}$ terms represent the effect of misalignment with respect to the $q = m/n$ surface, with G_H taken from equation (29) of reference [34] and G_{cd} approximated by

$$G_{cd} = (1+G_{coeff})\frac{[1-\tanh(\frac{0.75x_{norm}-0.3}{0.2})]}{[1-\tanh(\frac{-0.3}{0.2})+2x_{norm}^3]} - G_{coeff}\exp(-G_{exp}x_{norm}^2). \quad (7)$$

$G_{coeff} = 0.6$ and $G_{exp} = 1$ have been used based on figure 2 of reference [33] for $w/w_{dep} \approx 1$ as the ones involved here; the form of G_{cd} used in the simulations will be discussed in more details along with the experimental and simulation results in section 2.3; x_{norm} quantifies the misalignment level of EC beams with respect to the rational surface and is defined by

$$x_{norm} = \frac{|\overline{\rho}_{dep} - \overline{\rho}_{mn}|}{max(w, w_{dep})}. \tag{8}$$

The classical stability index $\overline{\rho}_{mn}\Delta'$ can in principle be calculated from the equilibrium and effective q profile, but is very sensitive to the accuracy of equilibrium reconstruction as well as to the derivatives of q profiles and hard to be evaluated well. For simulations with the MRE, a typical approach is to use a constant medium value between marginal classical stability $\overline{\rho}_{mn}\Delta' = 0$ and strong stability $\overline{\rho}_{mn}\Delta' = -2m$ [1–3], thus $\overline{\rho}_{mn}\Delta' = -m$ assuming w is relatively large. As the w_{sat} without EC beams (i.e. $\Delta'_{CD} = \Delta'_H = 0$) is dominated by $\overline{\rho}_{mn}\Delta'_{BS}/\overline{\rho}_{mn}\Delta'$, a different value of $\overline{\rho}_{mn}\Delta'$ would require a different coefficient a_2 (thus $\overline{\rho}_{mn}\Delta'_{BS}$) to fit the experimental w_{sat}. For NTMs that are triggered by unstable q profiles (i.e. $\Delta' > 0$ at $w = 0$), as the ones here, the stabilizing effect of the modification of the current density by the island itself needs to be considered [17, 39] to simulate the full time evolution:

$$\overline{\rho}_{mn}\Delta' = \overline{\rho}_{mn}\Delta'_0 - \alpha\frac{w}{\overline{\rho}_{mn}}, \tag{9}$$

where $\overline{\rho}_{mn}\Delta'_0$ represents the stability at $w = 0$ and is positive at the time of triggering. A first approximation of α can be given by taking the lowest order terms from [39]:

$$\alpha \approx \frac{m^2a^2}{\overline{\rho}_{mn}^2}(1 - \frac{s_{mn}\overline{\rho}_{mn}}{ma}), \tag{10}$$

while ensuring $\alpha > 0$ by taking for example the maximum between equation (10) and m. It is possible to measure α through dedicated experiments as well. For example reference [17] gives $\alpha = \alpha_{[17]} \cdot \overline{\rho}_{mn} \approx 33[m^{-1}] \cdot 0.12[m] \approx 4$ in similar plasmas as used here. However, quasilinear effects resulting from the flattening of the current profile as the island develops have been found to be important [40], and we define here an ad-hoc model both considering these quasilinear effects and representing a stationary $\overline{\rho}_{mn}\Delta'$ value for large w as in previous simulations [2, 3, 20]:

$$\overline{\rho}_{mn}\Delta' = \overline{\rho}_{mn}\Delta'_0 - \frac{(\overline{\rho}_{mn}\Delta'_0 + \overline{\rho}_{mn}\Delta'_{sat})w}{\sqrt{w^2 + ((\overline{\rho}_{mn}\Delta'_0 + \overline{\rho}_{mn}\Delta'_{sat})\overline{\rho}_{mn}/\alpha)^2}}, \tag{11}$$

where $\overline{\rho}_{mn}\Delta'_{sat}$ represents the value at large w. In this case, equation (11) gives $\overline{\rho}_{mn}\Delta' = \overline{\rho}_{mn}\Delta'_{sat} = const$ (e.g. $const = -m$) for relatively large w and recovers equation (9) at small w.

Equation (11) allows simulating the entire island width evolution, starting from $w = 0$, given that $\overline{\rho}_{mn}\Delta'_0$ is specified as well. Based on the Δ'-triggered nature of the NTMs involved here (through strong near-axis co-ECCD depositions) [17, 18], $I_{cd,tot}$ is expected to play a role in $\overline{\rho}_{mn}\Delta'_0$ and we propose a simple analytical model for $\overline{\rho}_{mn}\Delta'_0$:

$$\overline{\rho}_{mn}\Delta'_0 = \overline{\rho}_{mn}\Delta'_{ohmic0} + k\frac{I_{cd,tot}}{I_p}, \tag{12}$$

where $\overline{\rho}_{mn}\Delta'_{ohmic0}$ refers to the stability index in case of no EC power (i.e. ohmic) and zero island width, $I_{cd,tot}$ stands for the total current driven by all EC beams (including both central and off-axis ones) and $k\frac{I_{cd,tot}}{I_p}$ (with $k > 0$) represents the modification of the stability by ECCD. Note that given the relatively short time scale on TCV and the strong co-ECCD involved here ($\frac{I_{cd,tot}}{I_p} \approx 40/110 \approx 36\%$), equation (12) accounts for the change of the linear stability through a global change of the q profile by ECCD regardless of the appearance of a mode. This is different from the effect of small local off-axis ECCD depositions on Δ' [41,42]. Interpretative simulations with ASTRA show that the magnetic shear at the 2/1 surface, s_{21}, increases with increasing $I_{cd,tot}$ (under constant I_p), which justifies equation (12) to some extent. More theoretical inputs are desired to model more accurately this dependence. The value of $\overline{\rho}_{mn}\Delta'_{ohmic0}$ is found to be related to density and is evaluated through dedicated experiments (e.g. EC power ramps under various density levels, density ramps, etc) and corresponding MRE simulations, together with the value of k. More details concerning this part will be presented in a separate paper.

2.3. Experimental and simulation results

Based on the experimental setup and MRE model presented above, this section discusses about several representative examples of the NTM control experiments on TCV as well as corresponding interpretative simulations with the MRE. Constraints on the theoretical model, ranges of the free parameters used in the simulation as well as underlying physics will also be detailed.

Section 2.3.1 presents a simple example of the self-stabilization of 2/1 NTMs through a slow ramp-down of the destabilizing power, which helps to define the threshold island width w_{de}; section 2.3.2 discusses about the evolution of a 2/1 NTM along with a large variation of the deposition location of the control beam (between the plasma center and edge), which constrains better the theoretical model used in the simulations; section 2.3.3 compares the effect of co-ECCD, counter-ECCD and ECH on the stabilization of 2/1 NTMs, quantifies various effects and defines the range of a_4 (equation (4), for $\overline{\rho}_{mn}\Delta'_{CD}$) and a_5 (equation (5), for $\overline{\rho}_{mn}\Delta'_{H}$) in the simulations; section 2.3.4 compares the efficiency of NTM prevention with NTM stabilization, in terms of the minimum EC power required in each case.

2.3.1. Self-stabilization: slow ramp-down of central co-ECCD power As a first example of the MRE model described in the previous section, the evolution of an EC-heated TCV discharge without active NTM stabilization is shown in figure 2. About 0.96MW of X2 EC power in total is turned on at $0.4s$ and deposits co-ECCD near the plasma center through two launchers ($L4$ and $L6$) in this test. A 2/1 NTM is triggered at about $0.5s$, 100ms (i.e. the resistive time) after switching on the EC power and is sustained. Starting from $1.2s$, the EC power is slowly ramped down and reaches a total power of about 0.35MW at $2.1s$ when the mode self-stabilizes. During the slow ramp-down of

the EC power, the island width slowly decreases (with a small negative growth rate $\frac{dw}{dt}$ as indicated by the dashed magenta curve in figure 5, color online) and quickly drops below the noise level from $w = 1.8cm$. This provides an estimation of $w_{de} \approx 1.8cm$ in the test (w_{de} here corresponds to the marginal island width as defined in reference [1]), which is in accordance with that calculated by equation (6).

To quantify the effects of various terms on the w evolution, simulations with the MRE model presented above have been performed. Constant coefficients have been used to simulate the entire shot: $w_{de} = 1.8cm$, $k = 6$, $\alpha = 5$, $\overline{\rho}_{mn}\Delta'_{sat} = -1.4$, $a_2 = 2.1$ and $a_3 = 0.25$. a_4 and a_5 are not discussed here since only near-axis EC beams are involved in this test, i.e. $\overline{\rho}_{mn}\Delta'_{CD} \approx 0$ and $\overline{\rho}_{mn}\Delta'_{H} \approx 0$. w_{dep} can be inferred from TORAY outputs, for instance, the example shown in figure 1 suggests a full e^{-1} width about $0.2 \times 25cm = 5cm$ for $L4$ and $L6$ while $w_{dep} \approx 3cm$ for $L1$ (note that $L1$ is not used in the experiment described here). w_{dep} can vary with varying deposition locations, but a fixed and constant $w_{dep} = 5cm$ has been used for all launchers for simplicity as well as considering the possible beam broadening effects [43, 44, and references therein] that are not included in TORAY.

To simulate the w evolution starting from $w = 0$, $\overline{\rho}_{mn}\Delta'_0$ is evaluated based on equation (12) and used by equation (11) to estimate the time-varying $\overline{\rho}_{mn}\Delta'$, as shown in figure 3. The full island width evolution is shown in figure 4, and one can see that the simulated island width (red, color online) fits well (within the experimental error bars) the measured width (blue), in terms of the triggering, the w_{sat} and the full stabilization. The green curve represents the β_p trace that dominates the $\overline{\rho}_{mn}\Delta'_{BS}$ term and is scaled based on a w_{ref} (typically w_{sat}) at a selected t_{ref}, i.e. $w_{scaled}(t) = \frac{\beta_P(t)}{\beta_p(t_{ref})} w_{ref}$. The $\frac{dw}{dt}(w)$ traces at several interesting time slices of the simulated island width evolution are shown in figure 5, while the dashed magenta curve is taken from the measured island width evolution. One can see that at $t = 0.5s$, $\frac{dw}{dt} > 0$ at $w = 0$ (due to a positive $\overline{\rho}_{mn}\Delta'$) and the mode starts to grow, representing the onset of the mode; at $t = 1s$, $\frac{dw}{dt} \approx 0$ at $w_{sat} = 5cm$; from $t = 1.2s$, the EC power is ramped down slowly and $\frac{dw}{dt} \approx 0$ is sustained with decreasing w_{sat}. The decrease of the central ECCD power has two main effects: it reduces $I_{cd,tot}$, changes the q profile and hence $\overline{\rho}_{mn}\Delta'$ (captured through equation (12)) as well as lowers the $\overline{\rho}_{mn}\Delta'_{BS}$ term that is sustaining the mode. At $t = 2.1s$, the maximum of $\frac{dw}{dt}$ goes just below 0 with $w = 1.8cm$ and the mode is fully stabilized; after turning off the EC power at $t = 2.25s$, the entire $\frac{dw}{dt}$ curve remains negative and the plasma is stable to NTMs.

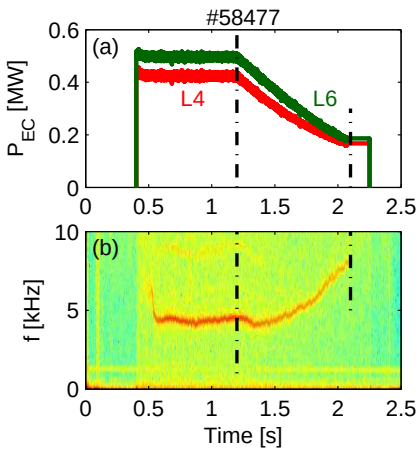

Figure 2: Experimental overview: (a) EC power traces, showing a slow power ramp-down from $1.2s$; (b) NTM spectrogram.

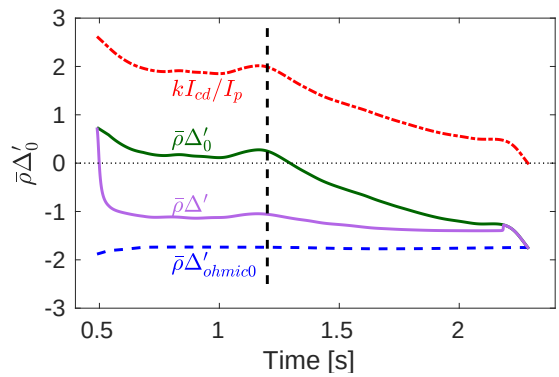

Figure 3: (Color online) Time-dependent $\overline{\rho}_{mn}\Delta'_0$ and $\overline{\rho}_{mn}\Delta'$ for #58477 (figure 2) based on equation (11) and (12): dashed blue - ohmic contribution; red dash-dot - contribution from ECCD; solid green - $\overline{\rho}_{mn}\Delta'_0$; solid purple - final $\overline{\rho}_{mn}\Delta'$ used.

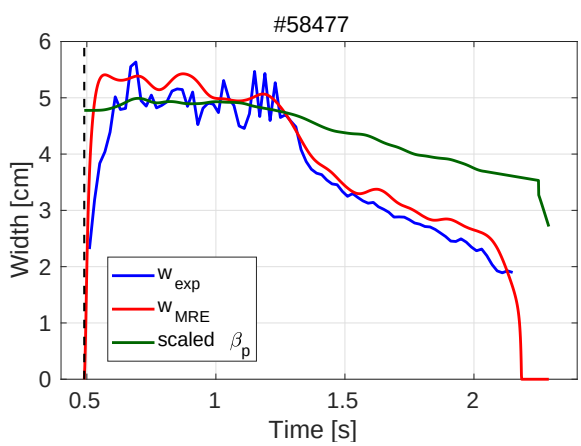

Figure 4: (Color online) Island width evolution for #58477 (figure 2): blue - measurement; red - simulation with MRE; green - β_p scaled onto the same plot.

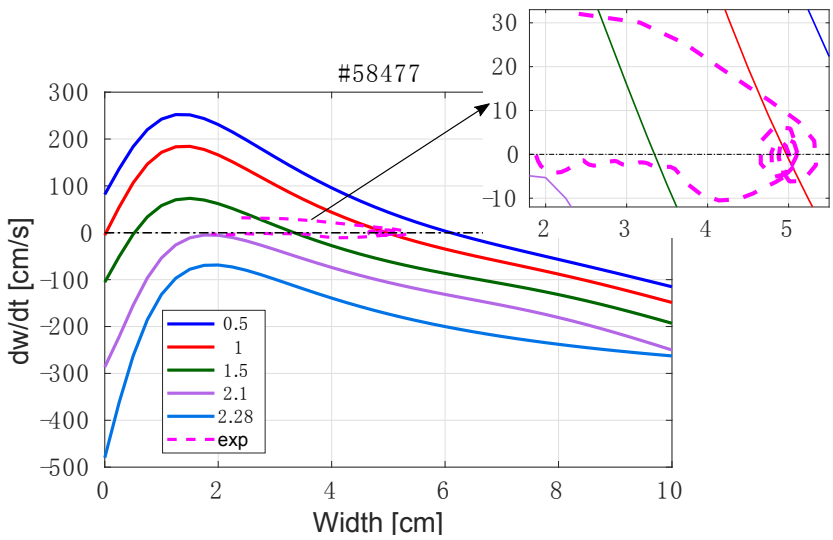

Figure 5: (Color online) $\frac{dw}{dt}(w)$ traces at several time slices of the simulated w evolution for #58477 (red curve in figure 4): NTM onset ($t = 0.5s$), $w_{sat} = 5cm$ ($t = 1s$), $w_{sat} = 3.5cm$ ($t = 1.5s$), self-stabilization ($t = 2.1s$) and ohmic plasma ($t = 2.28s$).

2.3.2. NTM stabilization with varying co-ECCD deposition location Highly reproducible NTM stabilization experiments have been carried out on TCV, showing strong stabilization effect when co-ECCD beams reach the target mode location. Shown in figure 6 is one example of such an experiment (TCV #56027). In this test, EC power is turned on at $0.4s$ and deposits co-ECCD near the plasma center through $L4$ and $L6$, which triggers a 2/1 NTM at about $0.5s$.

The control beam is switched on at $0.7s$ and deposits co-ECCD through a third launcher ($L1$) with 0.75MW power. As shown in figure 6 (b) and (c), the deposition location of $L1$ is varied, causing a variation of the mode amplitude and frequency. The radial location of the $q = 2$ surface based on the ASTRA output is indicated by the dashed black curve in figure 6 (b), as used in the simulations with the MRE. A partial stabilization effect can be seen when the EC beam reaches the mode location ($q = 2$ surface) for the first time at $t = 1.15s$. The mode amplitude recovers (but reaches a lower value) once the beam moves away (figure 9) and is fully stabilized when the beam crosses the $q = 2$ surface for the second time at $t = 1.53s$. $I_{cd,tot}$ then increases along with the movement of $L1$ from outside the $q = 2$ surface to the plasma center, but no mode is triggered again due to a decrease of n_{el} and a more stable $\overline{\rho}_{mn}\Delta'_{ohmic0}$ in equation (12).

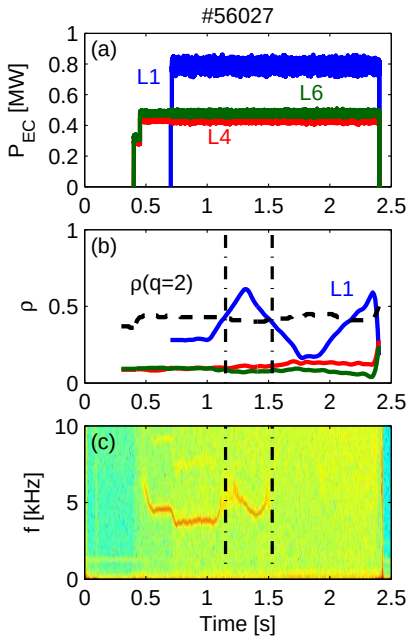

Figure 6: Experimental overview: (a) EC power trace; (b) EC deposition location; (c) magnetic spectrogram.

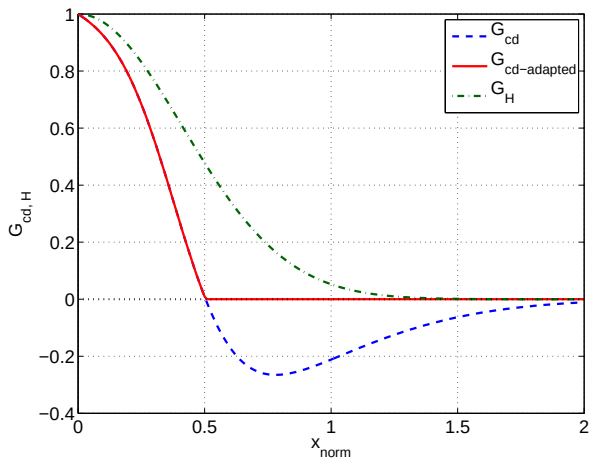

Figure 7: $G_{cd,H}$ terms with $w/w_{dep} = 1$: dashed blue - G_{cd} from theory; full red - adapted G_{cd} without the negative (destabilizing) part; dash-dot green - G_H from theory.

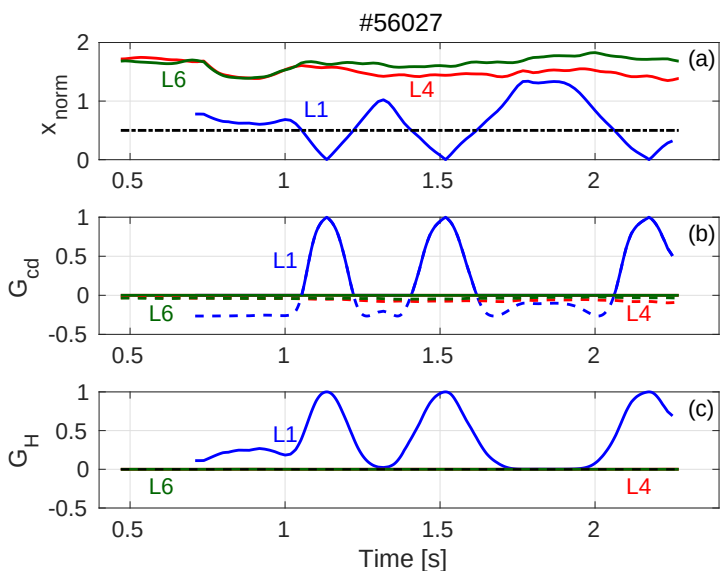

Figure 8: (Color online) Misalignment levels (x_{norm}) of the EC beams and the corresponding G_{cd} and G_H values for shot #56027 shown in figure 6: (a) solid - x_{norm} of EC beams from different launchers; dash-dot black - $x_{norm} = 0.5$, where the theoretical G_{cd} value changes its sign, as shown in figure 7; (b) G_{cd} of different beams: solid - evaluated based on the adapted G_{cd} curve in figure 7; dashed - based on the theoretical G_{cd} curve; (c) G_H evaluated based on equation (29) of reference [34].

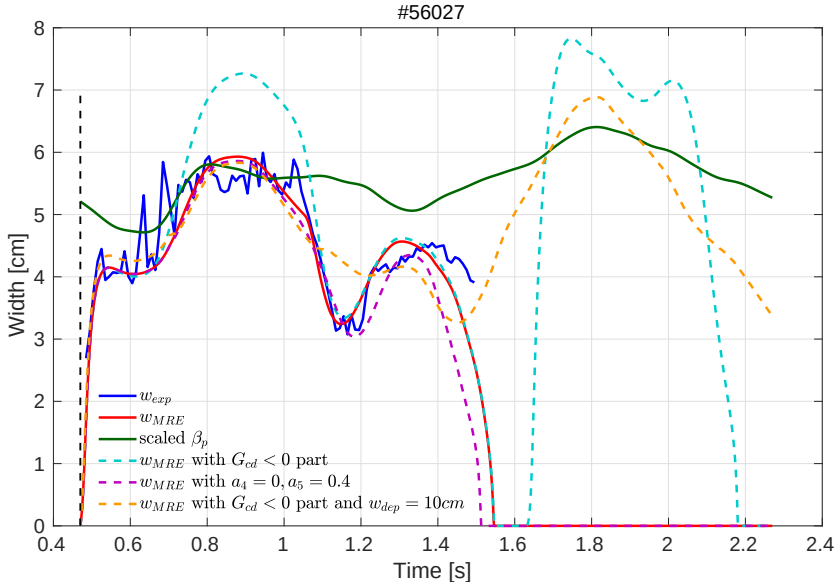

Figure 9: (Color online) Full island width evolution of #56027 (figure 6): blue - measurements; red - simulation with the adapted G_{cd} curve in figure 7 (i.e. without the negative part); green - β_p scaled onto the same plot; dashed cyan - simulation with the theoretical G_{cd} curve in figure 7; dashed purple - simulation with $a_4 = 0$ and $a_5 = 4$; dashed orange - simulation with the theoretical G_{cd} curve and $w_{dep} = 10cm$ for $L1$.

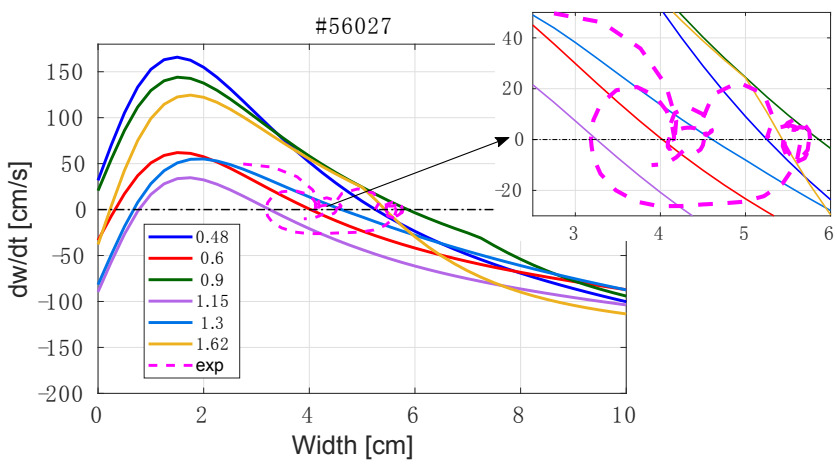

Figure 10: (Color online) $\frac{dw}{dt}(w)$ traces at several time slices of the best-fit case for #56027 (red curve in figure 9): NTM onset ($t = 0.48s$), $w_{sat} = 4cm$ ($t = 0.6s$), $w_{sat} = 6cm$ ($t = 0.9s$), partial stabilization ($t = 1.15s$), full stabilization ($t = 1.3s$) and EC-heated plasma without mode ($t = 1.62s$). The dashed magenta curve is taken from the measured w evolution (solid blue curve in figure 9, with extra smoothing to calculate $\frac{dw}{dt}$), showing the fast increase of w from $2.8cm$ to $4.2cm$, the saturation at $w \approx 4.2cm$ and $w \approx 5.5cm$, the drop from $w \approx 5.5cm$ to $w \approx 3.2cm$, the recovery to $w \approx 4.5cm$ and the stabilization.

Simulations with the MRE have been performed and it is necessary to specify $\overline{\rho}_{mn}\Delta'_{CD}$ and $\overline{\rho}_{mn}\Delta'_{H}$ since small values of x_{norm} (thus large G_{cd} and G_H) are covered along with the movement of $L1$. As described in section 2.2, G_H is taken from

reference [33] and G_{cd} approximated by equation (7). The shape of these two curves are shown in figure 7 for $w/w_{dep} \approx 1$ as the ones involved here. As depicted by the dashed blue curve, the theoretical G_{cd} is characterized by a strong negative (destabilizing) part for large beam misalignment ($x_{norm} \geq 0.5$). However, similar to #56027 shown here, no such destabilizing effects have been observed experimentally so far in the numerous NTM stabilization tests with varying EC beam deposition locations on TCV. For example, the experiments presented in reference [11] (its figure 1, 3 and 4) demonstrate full NTM stabilization when the ρ_{dep} of the control co-ECCD beam reaches close enough to the mode location ($x_{norm} < 0.5$) from either inside or outside the $q = m/n$ surface. As shown in figure 3 of reference [11] (#40411 and #40418), near monotonic decreases of the measured island widths are observed along with the movement of the control beams from $x_{norm} > 0.5$ to $x_{norm} < 0.5$, without any local increases of w, which does not seem to support the predicted $G_{cd} < 0$ part. This phenomenon (as observed in other experiments) may be explained by the finite or even strong heating contribution from the EC beams (i.e. $\overline{\rho}_{mn}\Delta'_H$) in present-day tokamaks [33, 45] that counteracts this destabilizing effect. It may also be that the destabilizing effect, if any, is not as strong as predicted by theory.

To better clarify this phenomenon and isolate the effect of the negative part of G_{cd} on the island evolution, an adapted G_{cd} curve (red curve in figure 7) has been tested as well in the simulations, removing the $G_{cd} < 0$ part while retaining the same stabilizing effect. For the experiment illustrated in figure 6 (#56027), the x_{norm} (equation (8)) of different launchers as well as the corresponding G_{cd} and G_H levels are depicted in figure 8, where the dashed lines in figure 8 (b) represents the level of G_{cd} considering the negative part. Note that G_{cd} and G_H (solid curves) are very small at $t = 1s$ and $t = 1.3s$ when $L1$ just starts to move towards the mode location, so the control beam does not have obvious effects on the mode evolution until $t \approx 1.1s$ and $t \approx 1.4s$ respectively, when the beam is close enough to the mode location. This is in accordance with the observed mode evolution in figure 6 and 9. Similar to #58477 (figure 2 - 5), constant coefficients have been used in simulating the entire w evolution (from $w = 0$): $w_{de} = 2.1cm$, $k = 6$, $\alpha = 5$, $\overline{\rho}_{mn}\Delta'_{sat} = -1.4$, $a_2 = 2.4$, $a_3 = 0.25$, $a_4 = 0.4$ and $a_5 = 1.5$. Among these, k, α, $\overline{\rho}_{mn}\Delta'_{sat}$ and a_3 remain exactly the same as in #58477, while a slightly different w_{de} is used due to different transport conditions and a slightly different a_2 to fit the maximum experimental w_{sat}. The range of a_4 and a_5 is summarized in equation (15) and table 1 through detailed NTM stabilization experiments with co-ECCD, counter-ECCD and ECH beams as well as corresponding simulations, as will be discussed in the next section. Within that range and with the adapted G_{cd} curve (i.e. removing the destabilization effect), $a_4 = 0.4$ and $a_5 = 1.5$ provide the best fit of this experiment so far, as shown by the solid red curve (color online) in figure 9.

This simulated w fits very well the entire w evolution, in terms of the triggering, the w_{sat}, the partial stabilization as well as the full stabilization. We emphasize that the above-mentioned coefficients are fixed during the entire discharge simulation. The $\frac{dw}{dt}(w)$ traces of this simulated w evolution are depicted in figure 10. With the same coefficients,

another simulation has been performed with the theoretical G_{cd} curve that includes the destabilizing effect, shown as the dashed cyan curve in figure 9. As indicated by the dashed curves in figure 8 (b), there are strong destabilizing effects of the EC beam (i.e. $G_{cd} < 0$) when depositing on both sides of the $q = 2$ surface (i.e. $0.7s \leq t \leq 1.05s$ and $1.22s \leq t \leq 1.4s$), causing a strong increase of w as seen from the dashed cyan curve in figure 9. Note that the product of the coefficients in front of G_{cd} (equation (4)) is larger when the beam deposits inside the $q = 2$ surface than outside, leading to a stronger destabilizing $\overline{\rho}_{mn}\Delta'_{CD}$ and explaining the significant increase of the simulated w only when $0.7s \leq t \leq 1.05s$ (dashed cyan curve). The destabilizing effect from G_{cd} also leads to a $\overline{\rho}_{mn}\Delta'_{CD} > 0$ at $1.62s \leq t \leq 2.05s$ when $L1$ is moving towards the plasma center and would have triggered the mode again, which is not observed in the experiment.

Efforts have been made to simulate the w evolution with the theoretical G_{cd} curve by tuning different parameters, e.g., a_4, a_5 and w_{dep}. For $w_{dep} = 5cm$, it is found that even with a very small ECCD effect ($a_4 = 0.05$) and very large heating term ($a_5 = 4$), the mode would have been triggered when $L1$ moves towards the plasma center. Reasonable fit of the measured w can be achieved with $a_4 = 0$ and $a_5 = 4$ (dashed purple curve in figure 9), but it is not physical as on one hand ECCD is expected to play a role (i.e. a_4 should be finite) and on the other hand $a_5 = 4$ is already out of the range of a_5 defined in the next section (equation (15)). Doubling the w_{dep} of $L1$ (i.e. $w_{dep} = 10cm$) and using $a_4 = 0.1$ and $a_5 = 2$, the destabilizing effect from the $G_{cd} < 0$ part (i.e. with $\overline{\rho}_{mn}\Delta'_{CD} > 0$) when $L1$ is largely misaligned can be marginally compensated by the stabilizing $\overline{\rho}_{mn}\Delta'_{H}$ and $\overline{\rho}_{mn}\Delta'_{GGJ}$ terms. However, with this wide w_{dep}, the simulated w evolution as shown by the dashed orange curve in figure 9, cannot recover the observed localized partial or full stabilization effects when $L1$ reaches the mode location.

Similar exercises have also been performed for the above-mentioned experiments in reference [11] (#40411 and #40418) with constant coefficients. Note that the full NTM stabilization from inside and outside the rational surface in those two experiments defines well the actual location of the ρ_{mn}, while the fast drop of the measured w before full stabilization determines the w_{de} in the experiments, as discussed in reference [11]. Detailed simulations suggest that the $G_{cd} < 0$ part of the theoretical curve would cause a sudden increase of the simulated w before full stabilization, especially for the case where the control beam moves from inside the rational surface (#40411) and thus having a larger product of the coefficients in front of G_{cd}. Even with a wide $w_{dep} = 10cm$ for the $\overline{\rho}_{mn}\Delta'_{H}$ term (while retaining the narrow w_{dep} for $\overline{\rho}_{mn}\Delta'_{CD}$) as well as the maximum $a_5 = 2.6$ from equation (15), the destabilizing effect from $G_{cd} < 0$ cannot be counteracted. This once again questions the existence or at least the level of the destabilization part in the G_{cd} curve, emphasizing the necessity of more theoretical investigations in this respect, in particular including the self-consistent modifications of the q profile on the transport and current redistribution time scales.

Given the large heating effects entangled in the experiments and the uncertainties in the measurement of w, it is not accessible to quantify the level of the negative part of G_{cd} (if any) in more details yet, but we have shown that it is not dominant in our

experiments and the adapted G_{cd} curve (without the negative part) will be used in all the following discussions for simplicity. It should also be noted that although tuning the fixed free coefficients does allow matching the largest experimental w_{sat}, the good match of the entire time evolution of w means that the parametric dependencies of the various terms used in the MRE match well the experimental results.

2.3.3. NTM stabilization with co-ECCD, counter-ECCD or ECH To better separate the contribution of heating ($\overline{\rho}_{mn}\Delta'_H$) and current drive ($\overline{\rho}_{mn}\Delta'_{CD}$) to 2/1 NTM stabilization in the test discharges, a series of NTM stabilization experiments have been carried out with the control beam in co-ECCD, counter-ECCD or ECH, respectively. As shown in figure 11, about 0.96MW of X2 EC power is switched on at $0.4s$ and deposits co-ECCD near the plasma center through $L4$ and $L6$. 2/1 NTMs are triggered at about $0.5s$, similar to the previous examples. $L1$ with a power of 0.75MW is switched on at $0.8s$ and moved towards the mode location from $t = 1s$ to stabilize the modes. The toroidal angle of $L1$ is set such that it can drive co-ECCD (#56171, figure 11 (a)-(c)), counter-ECCD (#56172, figure 11 (d)) or ECH (#56173, figure 11 (e)), respectively, while the poloidal angle remains the same for the three shots. $L4$ and $L6$ stay at the plasma center with a slow ramping down of their power from $0.9s$ and reach a total power of 0.6MW at $t = 2.25s$, which would still sustain the mode if $L1$ were not present, as indicated by the example shown in figure 2. For the case with co-ECCD (figure 11 (c)), the 2/1 NTM is fully stabilized at $t = 1.25s$ when $L1$ crosses the mode location for the first time. Note that $L1$ then continues depositing around the $q = 2$ surface and no mode is destabilized. For the case with counter-ECCD (figure 11 (d)) and similar amount of driven current as in the co-ECCD case, partial stabilization effect can be observed. For the case with ECH, partial stabilization is kept until $t = 2.37s$, when the $L1$ beam reaches the mode location for the third time and fully stabilizes the mode just before turning off the EC power at $t = 2.4s$, as illustrated in figure 11 (e).

It is interesting to determine the relative importance of heating ($\overline{\rho}_{mn}\Delta'_H$) and current driven ($\overline{\rho}_{mn}\Delta'_{CD}$) on the mode evolution by simulating these three shots with the MRE. To better quantify the accuracy of each simulation, we define a cost function χ:

$$\chi^2 = \frac{1}{N}\sum_{i=1}^{N}\left(\frac{w_{sim}(t_i) - w_{measure}(t_i)}{w_{measure}(t_i)}\right)^2 \tag{13}$$

for simulations without involving any full stabilization, and

$$\chi^2 = \frac{1}{M}\sum_{i=1}^{M}\left(\frac{w_{sim}(t_i) - w_{measure}(t_i)}{w_{measure}(t_i)}\right)^2 + c_{weight}\left(\frac{t_{stab,sim} - t_{stab,measure}}{t_{norm}}\right)^2 \tag{14}$$

for simulations involving full NTM stabilization and the time after. N here refers to the total number of measurement points within the simulation time window, $w_{sim}(t_i)$ the simulated island width evaluated at the measurement time point t_i, $w_{measure}(t_i)$ the measured w at t_i; M stands for the total number of measurement points at which $w_{sim}(t_i) \geq min(w_{measure}(t_{i=1,2,...,N}))$; $t_{stab,measure}$ refers to $100ms$ after the mode drops

below the noise level of magnetic measurements, which is about the time for w to reach 0 from the noise level as seen in figure 13; $t_{stab,sim}$ is the time at which w_{sim} reaches 0 again after onset; $c_{weight} = 1.8$ and $t_{norm} = 1s$ are chosen such that a $\Delta t = |t_{stab,sim} - t_{stab,measure}| = 0.15s$ offset in the stabilization timing would lead to a $\chi \geq 20\%$. Equation (14) is defined so that χ is not affected by "earlier" or "later" stabilization in the simulations as long as Δt is the same.

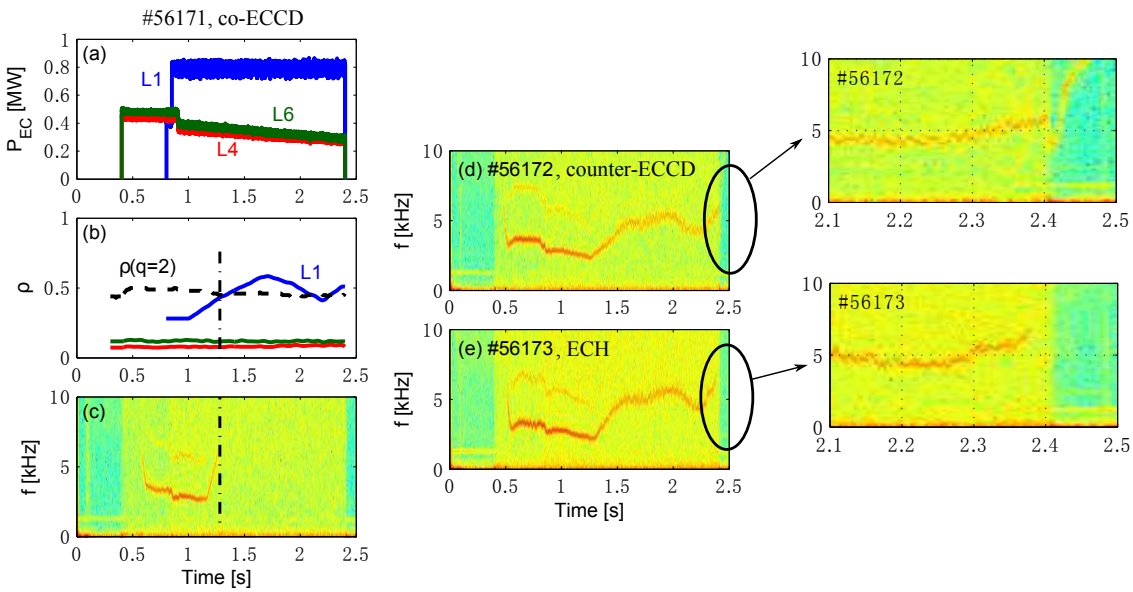

Figure 11: Experimental overview: (a) EC power traces (same in the three shots, power off at $t = 2.4s$); (b) EC deposition locations (same poloidal angles, similar deposition locations and $q = 2$ surface locations in the three shots); (c) magnetic spectrogram for #56171 ($L1$ in co-ECCD), full stabilization with the first crossing of the mode location at $t = 1.25s$; (d) magnetic spectrogram for #56172 ($L1$ in counter-ECCD), partial stabilization; (e) magnetic spectrogram for #56173 ($L1$ in ECH), full stabilization with the third crossing of mode location at $t = 2.37s$.

Simulations with the MRE model have been performed for these three shots and constant coefficients have been used to simulate the entire w evolution (from $w = 0$) in all cases: $k = 6$, $\alpha = 5$, $\overline{\rho}_{mn}\Delta'_{sat} = -1.4$ and $a_3 = 0.25$ remain exactly the same as in previous examples; $w_{de} = 1.9cm$ is used in the three shots; $a_2 = 1.5$ (#56171), 1.6 (#56172) and 1.6 (#56173) are used to fit the experimental w_{sat}, respectively; a_4 and a_5 are determined by optimizing χ of the three shots, as will be discussed below.

The range of a_5 can be determined by simulating #56173 (i.e. $L1$ in ECH) as $\overline{\rho}_{mn}\Delta'_{CD} \approx 0$ in this case, and we get

$$0.6 \leq a_5 \leq 2.6 \tag{15}$$

to keep $\chi \leq 20\%$ and thus within the error bar of island width measurements.

The best fit achieved for this shot is with $a_5 = 1.5$ and $\chi \approx 7.3\%$, as shown by the solid red curve (color online) in figure 12 (a). The simulation shows stronger oscillations along with the movement of $L1$ than the measurements, suggesting a possibly larger w_{dep}

than used here, although the simulation is still within the error bar of the measured island width. Doubling the w_{dep} of $L1$ ($10cm$ instead of $5cm$) and keeping the same coefficients (except a_5=2.2 instead of 1.5), a better fit ($\chi \approx 5.3\%$) can be achieved, as indicated by the dashed red curve in figure 12 (a). This suggests a possibly stronger broadening of the beam in this near perpendicular injection (ECH), though the details of which are out of the scope of this paper. Note that the slight ramp-down of the central power used for triggering NTMs ($L4$ and $L6$, with the minimum total power around 0.6MW) while keeping a constant power of the control beam $L1$ in these three experiments is not able to fully stabilize the NTMs, as indicated by the dashed cyan curves (color online) in figure 12 and 13, where the simulations are performed assuming no stabilization effect from $L1$ and the mode would have stayed. This is consistent with the example shown in figure 2, where the self-stabilization is only achieved when the total central power ramps down to around 0.35MW.

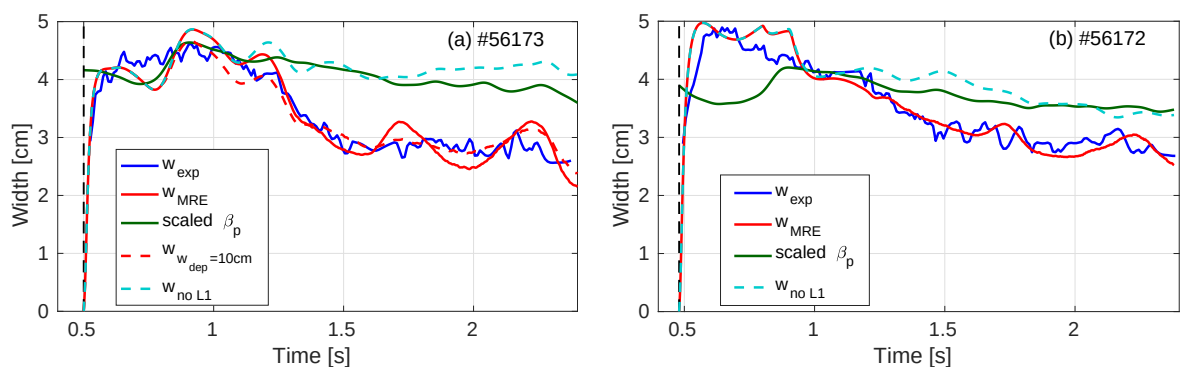

Figure 12: (Color online) Entire island width evolution: blue - measurements; red - simulations with MRE (best fits, both with $a_4 = 0.4$ and $a_5 = 1.5$); green - β_p scaled onto the same plot; dashed cyan: simulations assuming no stabilization effect from $L1$; dashed red in (a) - simulation assuming $w_{dep} = 10cm$ for $L1$.

With a fixed value of a_5 chosen from equation (15), the corresponding range of a_4 can be determined by simulating the co-ECCD and counter-ECCD experiments respectively and ensuring $\chi \leq 20\%$ for both shots. Various a_5 values have been tested and the corresponding ranges of a_4 are summarized in table 1. Note that a_4 should be a finite value as $\overline{\rho}_{mn}\Delta'_{CD}$ is expected to play a role and the minimum of a_4 has been set to 0.1 in these simulations. With $a_5 = 1.5$ (best fit for the ECH case, #56173), $a_4 = 0.4$ gives the best fit for both #56171 and #56172 with $\chi \approx 5.8\%$ and $\chi \approx 6.2\%$ respectively, as depicted by the red curves in figure 12 (b) and 13. A summary of the constant parameters and coefficients used to simulate these three shots are listed in table 2.

In figure 12, the simulations assuming no stabilization effect from $L1$ (i.e. the dashed cyan curves) also highlight the different effects of heating ($\overline{\rho}_{mn}\Delta'_H$) and current drive ($\overline{\rho}_{mn}\Delta'_{CD}$) on NTM stabilization. Note again that both ECH and counter-ECCD have a stabilizing heating effect (i.e. $\overline{\rho}_{mn}\Delta'_H < 0$). The fact that there is a larger difference between the dashed cyan curve (i.e. no stabilizing effect from $L1$) and the

solid blue or red curve (i.e. with $L1$) in the case of ECH (#56173, figure 12 (a)) than in the case of counter-ECCD (#56172, figure 12 (b)) indicates that ECH is more effective than counter-ECCD on NTM stabilization, as expected (and similarly when simply comparing with the scaled-β_p curve in green). This is because counter-ECCD has a destabilizing current drive effect (i.e. $\overline{\rho}_{mn}\Delta'_{CD} > 0$), which counteracts its stabilizing heating effect ($\overline{\rho}_{mn}\Delta'_{H} < 0$) and displays an overall less effective stabilizing effect than the ECH case (i.e. with $\overline{\rho}_{mn}\Delta'_{H} < 0$ and $\overline{\rho}_{mn}\Delta'_{CD} \approx 0$). Simulations suggest a slightly large amplitude of the heating effect ($|\overline{\rho}_{mn}\Delta'_{H}|$) than current drive effect ($|\overline{\rho}_{mn}\Delta'_{CD}|$) in #56172 (counter-ECCD), which explains the overall stabilizing effect observed in this case.

Table 1: Ranges of a_4 with various a_5 values

Fixed a_5 chosen based on equation (15)	Range of a_4 to keep $\chi \leq 20\%$ for #56171	Range of a_4 to keep $\chi \leq 20\%$ for #56172	Overlapped ranged of a_4 to keep $\chi \leq 20\%$ for both shots
0.6	[0.55 2.8]	[0.1 0.45]	no overlap
1	[0.45 2.7]	[0.1 0.7]	[0.45 0.7]
1.5	[0.35 2.6]	[0.1 1]	[0.35 1]
2	[0.25 2.5]	[0.1 1.3]	[0.25 1.3]
2.6	[0.1 2.3]	[0.25 1.7]	[0.25 1.7]

Table 2: List of the key parameters used in the simulations for #56171 - #56173

shot#	$w_{de}[cm]$	$w_{dep}[cm]$	k	α	$\overline{\rho}_{mn}\Delta'_{sat}$	a_2	a_3	a_4	a_5	χ
56171	1.9	5	6	5	-1.4	1.5	0.25	0.4	1.5	5.8%
-	1.9	5	6	5	-1.4	1.5	0.25	0.35	2	6.3%
56172	1.9	5	6	5	-1.4	1.6	0.25	0.4	1.5	6.2%
-	1.9	8	6	5	-1.4	1.6	0.25	0.4	1.5	6%
56173	1.9	5	6	5	-1.4	1.6	0.25	0.4	1.5	7.3%
-	1.9	8	6	5	-1.4	1.6	0.25	0.4	2	5.2%
-	1.9	10	6	5	-1.4	1.6	0.25	0.4	2.2	5.3%

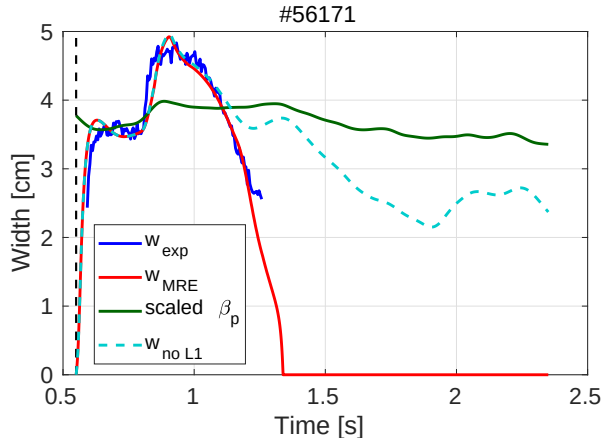

Figure 13: (Color online) Full island width evolution (#56171, figure 11): blue - measurements; red - simulation with MRE; green - β_p scaled onto the same plot; dashed cyan - simulation assuming no stabilization effect from $L1$.

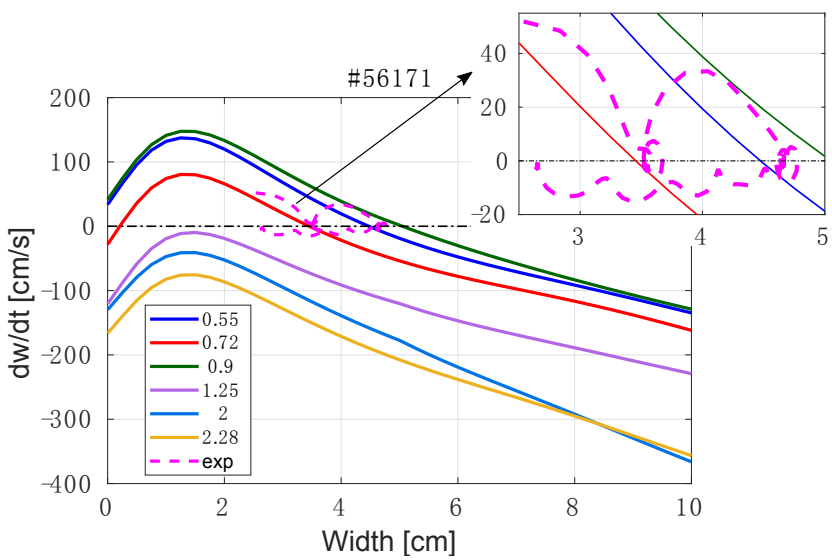

Figure 14: (Color online) $\frac{dw}{dt}(w)$ traces at several time slices of the simulated w evolution for #56171 (red curve in figure 13): NTM onset ($t = 0.55s$), $w_{sat} = 3.5cm$ ($t = 0.72s$), $w_{sat} = 5cm$ ($t = 0.9s$), full stabilization ($t = 1.25s$), EC-heated plasma without mode ($t = 2s$) and ohmic plasma ($t = 2.28s$).

For #56171 (figure 13), the dashed cyan curve confirms that it is the local current drive ($\overline{\rho}_{mn}\Delta'_{CD}$) and heating ($\overline{\rho}_{mn}\Delta'_{H}$) effects from $L1$ other than the ramp-down of the central power ($L4$ and $L6$) that fully stabilizes the mode at $t = 1.25s$, when the total central power reaches around 0.7MW and would still sustain the mode without $L1$. Complementary to the discussions of the counter-ECCD and ECH beam in the previous examples, the co-ECCD beam ($L1$) used in this experiment has $\overline{\rho}_{mn}\Delta'_{H} < 0$ and $\overline{\rho}_{mn}\Delta'_{CD} < 0$ (i.e. both stabilizing), thus exhibiting the strongest overall stabilization effect among the three experiments (#56171, #56172 and #56173).

To have an idea of the increase of the inductive (ohmic) current due to the deposition of EC powers in these experiments, it is feasible to use $\eta_H P_l$ from equation (5), where η_H estimates the efficiency with which the EC power is converted into a perturbative inductive current as defined in section 2.2 and P_l the absorbed EC power. For the relevance of the MRE, we have evaluated the $\eta_H P_l$ of the control beam $L1$, which gives 3kA $\sim$ 6kA in these three experiments. This is slightly lager than the current driven (I_{cd}) by the control beam $L1$ when it reaches the $q = m/n$ surface, which is 2kA $\sim$ 3kA in the case of co-ECCD (#56171). Note that there are some other parameters in front of $\eta_H P_l$ and I_{cd} for the calculation of $\overline{\rho}_{mn}\Delta'_H$ (equation (5)) and $\overline{\rho}_{mn}\Delta'_{CD}$ (equation (4)). Simulations suggest $\overline{\rho}_{mn}\Delta'_{CD} \leq \overline{\rho}_{mn}\Delta'_H < 0$ in the case of co-ECCD (#56171). Figure 14 shows the $\frac{dw}{dt}(w)$ traces at several interesting time slices of the best fit of #56171 (solid red curve in figure 13), concerning the triggering ($t = 0.55s$), $w_{sat} = 3.5cm$ ($t = 0.72s$), $w_{sat} = 5cm$ ($t = 0.9s$), full stabilization ($t = 1.25s$), EC-heated plasma without mode ($t = 2s$) as well as the ohmic plasma after turning off the EC power ($t = 2.28s$).

For the stabilization of NTMs with co-ECCD, it is useful to evaluate the current density driven at the mode location (i.e. $j_{cd}(\rho = \rho_{mn})$) as it is expected to compensate the missing bootstrap current density at the rational surface (i.e. $j_{bs}(\rho = \rho_{mn})$) caused by the mode. Following the conventions in the literature [2, 14, 44, 45], we define $\eta_{NTM} \equiv \frac{j_{cd}(\rho=\rho_{mn})}{j_{bs}(\rho=\rho_{mn})}$ to quantify this effect. The level of η_{NTM} of five TCV experiments are summarized in figure 15 to have an idea of the η_{NTM} required for 2/1 NTM stabilization in our experiments. In these discharges, a third co-ECCD beam was switched on after the onset of 2/1 NTMs for NTM stabilization, similar to the EC power settings in #56027 (figure 6 (a)) and #56171 (figure 11 (a)). Different deposition locations of the control co-ECCD beam have been covered in these tests, as indicated by the abscissa ($x_{norm,sign}$) of figure 15, where $x_{norm,sign} = \frac{(\overline{\rho}_{dep}-\overline{\rho}_{mn})}{max(w,w_{dep})}$ is similar to x_{norm} (equation (8)) but defined here to distinguish depositions on different sides of the $q = m/n$ surface. For example, one can see from figure 15 that the control co-ECCD beam of #56027, #56171 and #55106 deposits around the $q = m/n$ surface (with $-0.5 \leq x_{norm,sign} \leq 0.5$) and displays a peak of η_{NTM} (due to a peak in $j_{cd}(\rho = \rho_{mn})$) when reaching near the $q = m/n$ surface, as expected. In #58248 and #58249, however, the control co-ECCD beam deposits far from the $q = m/n$ surface (by pre-program) with $x_{norm,sign} < -0.45$ (i.e. inside the rational surface, more towards the plasma center) and $x_{norm,sign} > 0.45$ (i.e. outside the rational surface, more towards the plasma edge), respectively. #58248 and #58249 thus have very small $j_{cd}(\rho = \rho_{mn})$ and η_{NTM}.

Full stabilization of 2/1 NTMs are only observed in #56027 and #56171, as marked by open circles with corresponding colors in figure 15 (color online). This suggests $\eta_{NTM} > 0.45$ for full 2/1 NTM stabilization in these experiments on TCV, with the perturbed bootstrap current density of the order of 10^5A/m^2. This η_{NTM} value is lower than the predicted requirement for ITER [2, 14, 44], which does not consider $\overline{\rho}_{mn}\Delta'_H$ explicitly in the calculations as $\overline{\rho}_{mn}\Delta'_{CD}$ is predicted to dominate in ITER [33, 34]. As suggested by the MRE simulations in this section, the amplitude of $\overline{\rho}_{mn}\Delta'_H$ is comparable to that of $\overline{\rho}_{mn}\Delta'_{CD}$ in our experiments with co-ECCD, contributing significantly to the

stabilization of NTMs and reducing the requirement of η_{NTM} for full NTM stabilization. Similar and lower values of η_{NTM} have been observed in other tokamaks [16] and are consistent with theoretical predictions considering $\overline{\rho}_{mn}\Delta'_H$ explicitly [45].

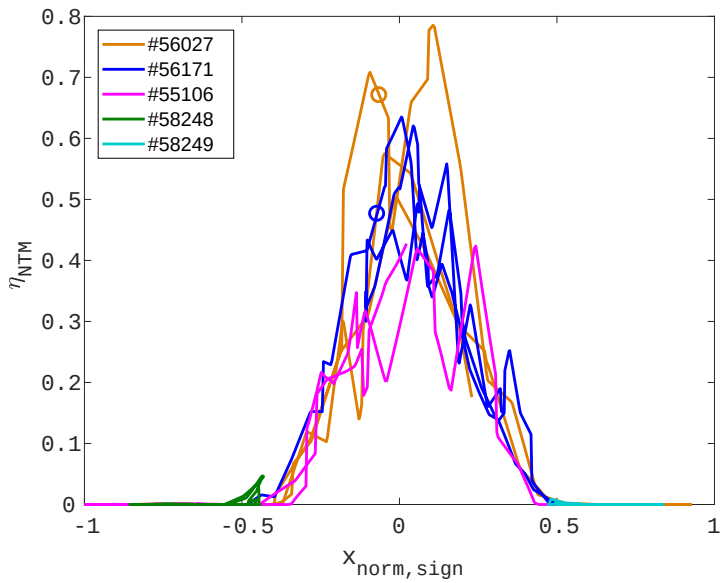

Figure 15: (Color online) A collection of the $\eta_{NTM} \equiv \frac{j_{cd}(\rho=\rho_{mn})}{j_{bs}(\rho=\rho_{mn})}$ reached in various 2/1 NTM stabilization experiments on TCV. The $x_{norm,sign}$ indicates the deposition location of the control beam with respect to the 2/1 rational surface. The two open circles represent the instances with full stabilization (in #56027 and #56171), which suggests $\eta_{NTM} > 0.45$ is required to fully stabilize 2/1 NTMs in these experiments on TCV. Note that in #58248 and #58249, the large misalignment level ($|x_{norm,sign}| > 0.45$) of the control beams was programmed on purpose.

2.3.4. NTM prevention versus stabilization As a method of NTM control, the prevention of NTMs is explored on TCV as well. In principle this allows avoiding NTMs altogether and can be the preferred control method, but note that it penalizes the Q factor and may be prohibitive for some scenarios [2]. An example of the NTM prevention tests is shown in figure 16, where $L1$ is switched on at $t = 0.3s$ and sweeps around the 2/1 rational surface sinusoidally. The small sinusoidal sweeping of the control beam ($L1$) is applied to facilitate the comparison between NTM prevention and stabilization (#58254, figure 17), by increasing the chance of covering the correct location in both cases, despite of possibly different plasma evolutions. As shown in figure 15, covering $x_{norm} \approx 0$ is a crucial parameter. $L4$ and $L6$ are switched on at $t = 0.4s$ and deposit near the plasma center with their full power to trigger NTMs, as used in previous examples presented in section 2.3.1 to 2.3.3. All the launchers are set to drive co-ECCD in this experiment. A ramp-down of $L1$ (i.e. the control beam) power is applied to determine the minimum power required for NTM prevention (i.e. without the onset of NTMs). It can be seen from figure 16 that no 2/1 NTMs are triggered until turning off $L1$ completely at $t = 1s$ when $L1$ power ramps down to 0.36MW, meaning that 2/1 NTMs

are successfully prevented with only 0.36MW.

In a comparable stabilization test shown in figure 17, similar plasmas and settings as in #58256 have been used, except that $L1$ is turned on after NTM onset and with a ramp-up of its power to determine the minimum power required for full NTM stabilization. In this test, the mode cannot be fully stabilized even with 0.75MW. These power levels suggest a higher efficiency of NTM prevention than stabilization, in terms of the EC power required in each case, similar to observations on other tokamaks [13]. However, prevention of NTMs may require a much longer temporal duration of the EC power and thus a larger total input energy than NTM stabilization, which needs to be taken into account in the trade-off and the selection of NTM control strategies. Note that the successful NTM prevention with sinusoidal sweeping (misalignment) around the rational surface also support the use of the adapted G_{cd} term (figure 7) in the simulations. Further experiments with different but constant EC powers for NTM prevention and stabilization are foreseen to better quantify their comparison.

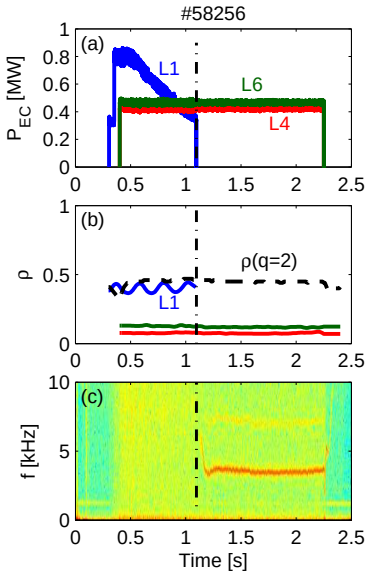

Figure 16: Overview of the NTM prevention test: (a) EC power traces; (b) EC deposition locations, with $L1$ sweeping sinusoidally around the mode location; (c) magnetic spectrogram showing the appearance of a 2/1 NTM ($\sim$ 4kHz) and its 2nd harmonic ($\sim$ 8kHz).

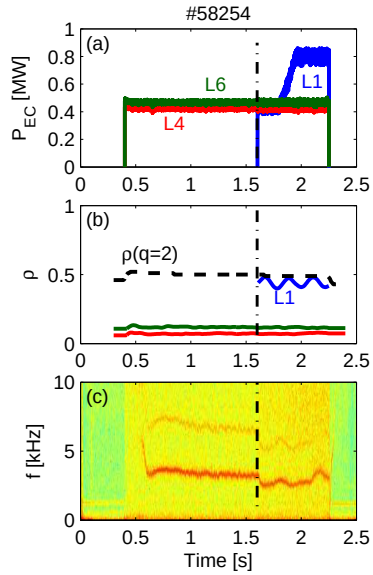

Figure 17: Overview of the NTM stabilization test: (a) EC power traces; (b) EC deposition locations, with $L1$ sweeping sinusoidally around the mode location; (c) magnetic spectrogram showing the appearance of a 2/1 NTM ($\sim$ 4kHz) and its 2nd harmonic ($\sim$ 8kHz).

Simulation results of the NTM prevention experiment (#58256) are shown in figure 18, starting from $t = 0.25s$ (i.e. ohmic plasma before turning on the EC power) with $w = 0$. Constant coefficients have been used in the simulations, with exactly the same values as listed in table 2 (the cases with $w_{dep} = 5cm$, $a_5 = 1.5$ and $a_4 = 0.4$), except with $a_2 = 2$ to better fit the experimental w_{sat}. The simulated red curve (color online) fits

very well the timing of NTM onset, the island saturation after NTM triggering as well as the fast self-stabilization after turning off the on-axis EC powers. The prevention effect is found to result from the local effects of off-axis co-ECCD (with $\overline{\rho}_{mn}\Delta'_{CD} \leq \overline{\rho}_{mn}\Delta'_{H} < 0$) as well as the favorable curvature ($\overline{\rho}_{mn}\Delta'_{GGJ} < 0$) that all together counteracts the positive $\overline{\rho}_{mn}\Delta'_{0}$ that tends to trigger the mode. The $\frac{dw}{dt}(w)$ traces at several time slices are shown in figure 19 and one can see that at $t = 1.096s$ (green), $\frac{dw}{dt}$ goes just above 0 at $w = 0$ and leads to the onset of the NTM. To have an idea of the prevention effect, another simulation (dashed cyan curve) is shown in figure 18, assuming no prevention effects from $L1$. In this case the mode would have been triggered at $t = 0.5s$, 100ms after turning on $L4$ and $L6$ power, similar to the NTM onsets presented in the previous examples.

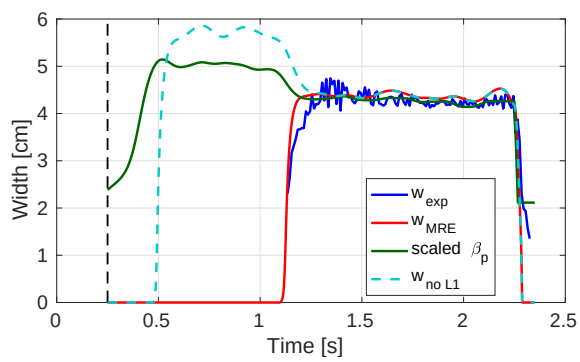

Figure 18: (Color online) Full island width evolution for #58256 (figure 16: blue - measurements; red - simulation with MRE; green - β_p scaled onto the same plot; dashed cyan - simulation assuming no prevention from $L1$.

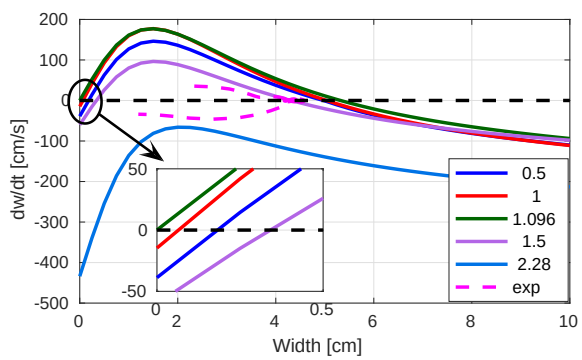

Figure 19: (Color online) $\frac{dw}{dt}(w)$ traces at several time slices of the simulated w evolution for #58256 (red curve in figure 18): Full prevention (no mode, $t = 0.5s$ and $t = 1s$), NTM onset ($t = 1.096$), $w_{sat} = 4.5cm$ ($t = 1.5s$), and ohmic ($t = 2.28s$).

3. Real-time multi-actuator control

3.1. A generic task-based multi-actuator control framework

The knowledge gained from the dedicated NTM studies shown in the previous section has facilitated the development of a reliable and efficient NTM control scheme. This in turn contributes to the design of a generic NTM controller that can be readily integrated in a plasma control system (PCS). For complex experiments on long-pulse tokamaks, it is crucial that the PCS can fulfil multiple control objectives with only a limited set of actuators. To this aim, a new generic PCS architecture has been proposed, implemented and tested experimentally on TCV [21,22]. As shown in figure 20, in the new framework, the PCS is separated into an interface and a tokamak-agnostic layer. The interface layer translates tokamak-specific signals from actuators and diagnostics into generic ones to be used by the tokamak-agnostic layer, and vice versa. For example, a plasma and actuator state reconstruction block uses RT diagnostics as well as RT simulations to

generate a generic continuous-valued representation of the state of both plasma and actuators. Specifically, RT analyses of magnetic perturbations have been used to provide estimations of mode type, amplitude and frequency [46], the RAPTOR observer [47] to reconstruct electron temperature and profiles, the RAPDENS-observer [48] to estimate density profiles and RT-TORBEAM [49, 50] to calculate EC beam depositions. This continuous-valued state is then translated by a generic plasma state monitor into a discrete finite-state representation of the conditions in plasma, with state transitions triggered on user-defined thresholds [21].

A task-based approach is implemented inside the tokamak-agnostic layer [22], providing a layer of abstraction for operators as they only have to specify control tasks, without having to consider the functionality of each controller. Based on the defined tasks, the discrete state and the pulse schedule, a generic supervisory controller [21] activates relevant tasks/controllers, prioritizes various tasks, and communicates the parameters specific to each control task. A task-based actuator manager [22] optimizes the actuator allocation for each task based on the plasma state, the actuator state and limits, the task priority and the resource requests per task from the controllers.

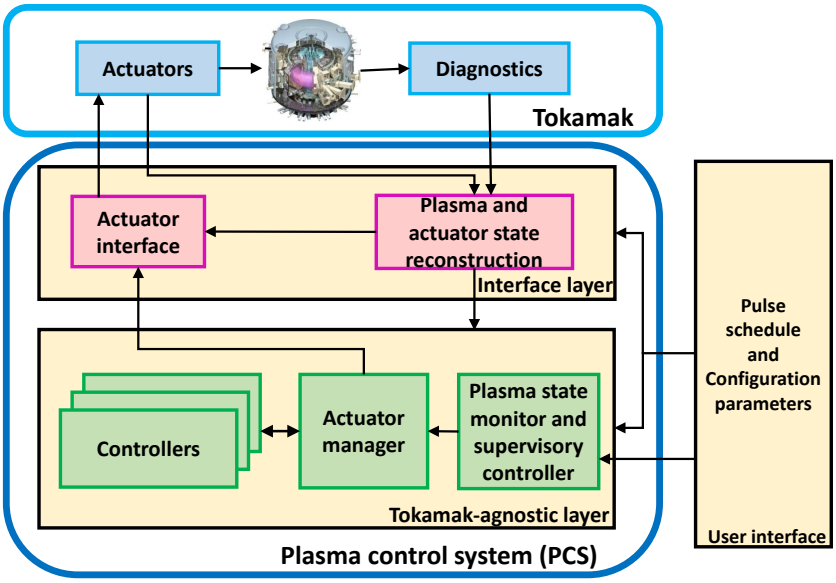

Figure 20: Overview of the generic plasma control system (PCS) framework [21, 22].

In this framework, it is important that controllers are generic as well and do not require knowledge of specific scenarios. For instance, the NTM controller should be able to perform its tasks requiring only the type of EC to use (i.e. co-ECCD) and knowing the m and n number of the mode to control, the presence, width and frequency of the mode, and possibly some standard plasma parameters like T_e and n_e that can be used to predict the mode evolution and compute the required power for NTM control by solving the MRE inside the control system in RT. This generic and versatile NTM controller is able to carry out all the NTM control experiments mentioned in section 2.3 and has been included in the integrated control test that will be discussed below.

3.2. RT integrated control of NTMs, β and model-estimated q profiles on TCV

The generic PCS framework has been successfully implemented on TCV. Using the first version of the system, with generic controllers and a preliminary actuator manager, RT integrated control of NTMs, β and model-estimated q profiles has been demonstrated on TCV. The details of various β and q profile controllers have been presented in references [23–25], and here we only concentrate on the generic NTM controller. As shown in figure 21 and preliminarily presented in reference [26], three EC launchers ($L1$, $L4$ and $L6$) are used to perform the three control tasks. Note that $L4$ and $L6$ share the same power source, so they always convey approximately the same power, while their deposition locations can be different as they have independent steering mirrors. In this experiment, $L4$ and $L6$ are set to drive co-ECCD with a nominal power of 0.5MW each and can be assigned to the three tasks based on their RT priority, while $L1$ with a nominal power of 0.75MW is set to drive counter-CD and is reserved for β and q profile control. The EC power of a certain launcher during its movement (e.g. toward the mode location for NTM control) is reduced to its minimum to minimize the perturbations exerted on other control tasks. Note that due to the absence of internal current density measurements on TCV, the q profiles used in these tests are estimations provided by RAPTOR [51, 52].

In this experiment, EC power is switched on at time point ① with all three launchers depositing near plasma center following feedforward EC commands, while RT control starts from ②. A 2/1 NTM is triggered at ③ and NTM control is activated and gets the highest priority. $L6$ is assigned to NTM control and moved toward the $q = 2$ surface to stabilize the mode. The NTM is fully stabilized at ④ when $L6$ reaches the mode location (figure 21 (d)). The power of $L6$ (thus $L4$ as well as they share the same power unit) is reduced to its minimum during the movement and recovers the requested value (0.5MW) once the deposition is close enough to the target position, as shown in figure 21 (a) and (d). A second 2/1 NTM is triggered at ⑤ and $L6$ is assigned again to NTM control and moved toward the mode location. Once the mode persists longer than a given time (one sweeping cycle in this case), $L4$ is also assigned to NTM control and moved toward the mode location (⑦), but not enough time is left in this shot for reaching the target position and fully stabilizing the mode. EC powers are turned off at ⑧ and the mode is self-stabilized. During the control of NTMs, β and q profile references cannot be followed very well due to limited power available for β and q profile control.

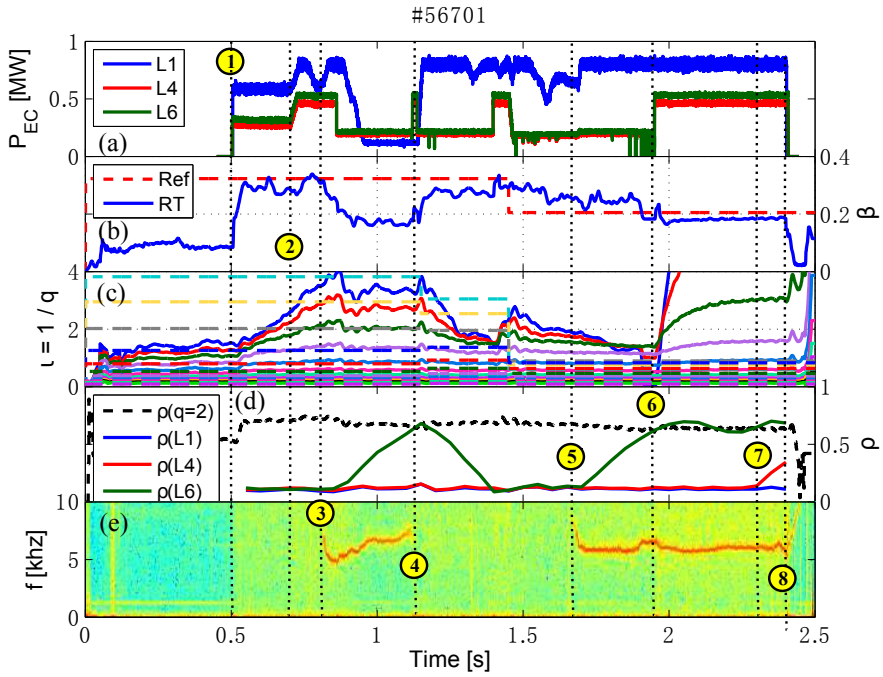

Figure 21: (Color online) Integrated control of NTMs, β and model-estimated q profiles on TCV: (a) EC power traces; (b) reference and RT β; (c) $\iota = q^{-1}$ profiles - different dashed/solid curves represent the reference/RT-estimated ι values at different radial locations; (d) deposition locations of different launchers, while the location of the $q = 2$ surface is indicated by the dashed black line; (e) magnetic spectrogram indicating the onset and stabilization of 2/1 NTMs. Various interesting time slices are highlighted by indexed vertical dotted lines, as detailed in the main texts.

It is worth mentioning that for more complex experiments on future long-pulse devices, it would be advantageous to have more "intelligent" controllers that are aware of the resources they will need to fulfill their tasks. For example, in the integrated control test shown here, the power requested to control a certain NTM is preset to be the nominal power of one launcher while reserving the ability to ask for more power (e.g. the nominal power of another launcher in the test) if the mode stays longer than a given time. A foreseen upgrade on the NTM control algorithm would be computing the amount of power required to stabilize or prevent an NTM in RT and predicting the mode evolution based on predictive modeling, e.g. with a RT version of the MRE model presented in section 2.2. This knowledge will facilitate the prioritization decisions made by the supervisory controller and the resource assignment made by the actuator manager, contributing to the overall integrated control scheme. The implementation of a RT-MRE in the PCS is left for future work.

4. Conclusions and outlook

Various aspects concerning the physics and control of 2/1 NTMs have been studied experimentally and numerically on TCV. The dynamic evolutions of 2/1 NTMs along

with varying deposition locations of the control beam have been studied in detail. The effect of co-ECCD, counter-ECCD and ECH on the stabilization of 2/1 NTMs has been compared through a series of experiments as well as interpretative simulations with the MRE. The prevention of 2/1 NTMs by means of preemptive ECCD has also been explored. As presented in section 2.3.4, a small sinusoidal sweeping of the radial deposition location of the EC power has been added to the control beam in two experiments to facilitate the comparison between NTM stabilization and prevention, by improving the coverage of the correct location in both cases despite of different plasma evolutions. It is shown that the prevention of NTMs is more efficient than NTM stabilization in terms of the minimum EC power required. In the interpretative simulations with the MRE, a simple analytical model has been proposed to evaluate the time-varying Δ', which allows one to simulate very well the entire island width evolution with the MRE, starting from zero width and including NTM prevention and stabilization for the first time, with very similar parameters.

It is worth emphasizing that the main goal of this work is not to propose a theoretical model for Δ', instead, it is to explore NTM physics and control strategies through dedicated experiments and interpretative simulations, finally contributing to the reliable and efficient integrated operations of tokamaks. The proposed simple analytical model for Δ', however, does allow simulating very well the entire island width evolution with MRE on TCV. Moreover, the MRE model used here contains also standard terms such as Δ'_{BS} and Δ'_H and have been tested not only for "seedless" NTMs (starting from $w = 0$) but also for standard seeded NTMs (starting from finite w). We have proposed a method to quantify the range of the free parameters that can be used in the simulations, in order to be able to compare their values with the expected values. We have shown that we could simulate the entire time evolution of the 2/1 island width for a rather complicated set of experimental cases (prevention, stabilization, sweeping, co-ECCD, counter-ECCD, ECH, etc) with very similar fixed coefficients. This has allowed the careful isolation of various effects and checking the (range of) validity of theoretical models, as detailed in section 2.3. In particular, our simulations explain the role of NTM prevention, for which Δ'_{CD} and Δ'_H take comparable part in our cases, and the role of sweeping. More theoretical inputs are needed to fully understand the proposed dependence of Δ'.

The reliable and efficient control of NTMs has facilitated the development of an NTM controller that is independent of the particular features of TCV and has been included in a generic PCS. With this PCS, integrated control of 2/1 NTMs, β and model-estimated q profiles has been demonstrated on TCV. As an outlook, a RT version of the MRE will be implemented in the PCS to compute the amount of power required to stabilize or preempt an NTM in RT and predict the mode evolution, contributing to the overall integrated control strategy.

Acknowledgments

The first author would like to thank Dr. D. Kim and Dr. S.H. Kim for providing the β and q profile controller involved in the integrated control experiment shown in this paper. This work has been carried out within the framework of the EUROfusion Consortium and has received funding from the Euratom research and training programme 2014-2018 and 2019-2020 under grant agreement No 633053. The views and opinions expressed herein do not necessarily reflect those of the European Commission. This work was supported in part by the Swiss National Science Foundation.

References

[1] Sauter O *et al* 2002 *Plasma Phys. Control. Fusion* **44** 1999
[2] Sauter O *et al* 2010 *Plasma Phys. Control. Fusion* **52** 025002
[3] La Haye R J *et al* 2006 *Nucl. Fusion* **46** 451
[4] Henderson M *et al* 2015 *Phys. Plasmas* **22** 021808
[5] Hegna C C and Callen J D 1997 *Phys. Plasmas* **4** 2940
[6] Brennan D P *et al* 2003 *Phys. Plasmas* **10** 1643
[7] Urso L *et al* 2010 *Nucl. Fusion* **50** 025010
[8] Février O *et al* 2016 *Plasma Phys. Control. Fusion* **58** 045015
[9] Février O *et al* 2017 *Plasma Phys. Control. Fusion* **59** 044002
[10] Yu Q *et al* 2004 *Phys. Plasmas* **7** 312
[11] Felici F *et al* 2012 *Nucl. Fusion* **52** 074001
[12] Humphreys D A *et al* 2006 *Phys. Plasmas* **13** 056113
[13] Nagasaki K *et al* 2005 *Nucl. Fusion* **45** 1608
[14] Zohm H *et al* 2007 *Plasma Phys. Control. Fusion* **49** B341
[15] Prater P *et al* 2007 *Nucl. Fusion* **47** 371
[16] Isayama A *et al* 2009 *Nucl. Fusion* **49** 055006
[17] Reimerdes H *et al* 2002 *Phys. Rev. Lett.* **88** 105005
[18] Lazzaro E *et al* 2015 *Nucl. Fusion* **55** 093031
[19] Ji X Q *et al* 2016 *Scientific Reports* **6** 32697
[20] Sauter O *et al* 1997 *Phys. Plasmas* **4** 1654
[21] Blanken T C *et al* 2019 *Nucl. Fusion* **59** 026017
[22] Vu N M T *et al* Tokamak-agnostic actuator management for multi-task integrated control with application to TCV and ITER *submitted to Fusion Eng. Design*
[23] Maljaars E *et al* 2017 *Nucl. Fusion* **57** 126063
[24] Vu N M T *et al* 2016 *Control Eng. Practice* **54** 34
[25] Mavkov B *et al* 2017 *Control Eng. Practice* **60** 28
[26] Kong M *et al* 2017 *44th EPS Conf. on Plasma Physics (Belfast, 26—30 June)* (http://ocs.ciemat.es/EPS2017PAP/pdf/P4.152.pdf)
[27] Matsuda K 1989 *IEEE Trans. on Plasma Science* **17** 6
[28] Schittenhelm M and Zohm H 1997 *Nucl. Fusion* **37** 1255
[29] Reimerdes H 2001 MHD stability limits in the TCV tokamak *EPFL PhD Thesis No.2399, Lausanne, Switzerland*
[30] Hofmann F 1988 *Comp. Phys. Communications* **48** 207
[31] Hawke J *et al* 2017 *Journal of Instrumentation* **12** C12005
[32] Pereverzev G V and Yushmanov P N 2002 *ASTRA: Automated System for Transport Analysis (Max-Planck-Institut für Plasmaphysik and Rep. IPP 5 vol 98)* (Garching: IPP)
[33] De Lazzari D *et al* 2009 *Nucl. Fusion* **49** 075002

[34] De Lazzari D *et al* 2010*Nucl. Fusion* **50** 079801
[35] Sauter O *et al* 1999 *Phys. Plasmas* **6** 2834
[36] Sauter O *et al* 2002 *Phys. Plasmas* **9** 5140
[37] Fizpatrick R 1995 *Phys. Plasmas* **2** 825
[38] Sauter O 2004*Phys. Plasmas* **11** 4808
[39] White R B *et al* 1977 *Phys. Fluids* **20** 800
[40] Pletzer A *et al* 1999 *Phys. Plasmas* **6** 1589
[41] Westerhof E *et al* 1990 *Nucl. Fusion* **30** 1143
[42] Westerhof E *et al* 2016 *Nucl. Fusion* **56** 036016
[43] Nikkola P *et al* 2003 *Nucl. Fusion* **43** 1343
[44] Poli E *et al* 2015 *Nucl. Fusion* **55** 013023
[45] Bertelli N *et al* 2011 *Nucl. Fusion* **51** 103007
[46] Galperti C *et al* 2017 *IEEE Trans. Nucl. Science* **64** 1446
[47] Felici F *et al*, "Real-time model-based plasma state estimation, monitoring and integrated control in TCV, ASDEX-Upgrade and ITER". Preprint: 2016 IAEA Fusion Energy Conference, Kyoto [EX/P8-33]
[48] Blanken T C *et al* 2018 *Fusion Eng. Design* **126** 87
[49] Poli E *et al* 2018 *Comp. Phys. Communications* **225** 36
[50] Reich M *et al* 2015 *Fusion Eng. Design* **100** 73
[51] Felici F *et al* 2011 *Nucl. Fusion* **51** 083052
[52] Felici F *et al* 2018 *Nucl. Fusion* **58** 096006